Journal of Materials Chemistry A

High performance thermoelectrics from low-cost and abundant CuS/CuI composites

Journal:	*Journal of Materials Chemistry A*
Manuscript ID	TA-ART-10-2023-006474.R1
Article Type:	Paper
Date Submitted by the Author:	12-Dec-2023
Complete List of Authors:	Mulla, Rafiq; BMS College of Engineering, Physics Živković, Aleksandar; Utrecht University Faculty of Geosciences, Department of Earth Sciences Warwick, Michael; Swansea University De Leeuw, Nora; University of Leeds, School of Chemistry; Utrecht University, Dept. of Earth Sciences Dunnill, Charlie; Swansea University, Chemistry Barron, Andrew; Swansea University, ESRI

High performance thermoelectrics from low-cost and abundant CuS/CuI composites

Rafiq Mulla[1,2‡*], Aleksandar Živković[3‡*], Michael E. A. Warwick[1], Nora H. de Leeuw[3,4], Charles W. Dunnill[1], Andrew R. Barron[1,5,6,7*]

[1] Energy Safety Research Institute, Swansea University, Bay Campus, Fabian Way, Swansea, SA1 8EN, UK
[2]Dept. of Physics, B.M.S. College of Engineering, Bengaluru-560019, India
[3] Department of Earth Sciences, Utrecht University, Princetonlaan 8a,3548CB Utrecht, The Netherlands
[4] School of Chemistry, University of Leeds, Leeds LS2 9JT, United Kingdom
[5] Arizona Institutes for Resilience (AIR), University of Arizona, Tucson, AZ 85721, USA
[6] Department of Chemistry and Department of Materials Science and Nanoengineering, Rice University, Houston, TX 77005, USA
[7] Faculty of Engineering, UniversitiTeknologi Brunei, Brunei Darussalam
[*]Corresponding Author: rafiq.mulla.phy@bmsce.ac.in (RM); a.zivkovic@uu.nl(AŽ)
c.dunnill@gmail.com (CWD); a.r.barron@swansea.ac.uk(ARB)
‡ These authors contributed equally

Abstract:

Materials with simultaneously excellent electrical conductivity (σ) and high Seebeck coefficient (S) are important for thermoelectric applications. However, obtaining such materials is a challenging task as σ and S vary inversely with respect to each other. Here, a new fabrication process has been demonstrated that produces composite materials with desired properties. Electrically highly conducting copper sulphide (CuS) particles are encapsulated within a compound with a high Seebeck coefficient, i.e. copper iodide (CuI), to form core-shell type composites. The presented results show that the concept of producing such composites allows the optimisation of both σ and S to provide enhanced thermoelectric performance (measured by the figure of merit, zT) when compared to the individual starting materials. Quantum mechanical calculations are performed to elaborate on the Schottky barrier formed at the interface between copper iodide and copper sulphide and elucidate aspects of the improved transport mechanism. Furthermore, an optimized compositional ratio between the respective composite parts is identified, which at the same time exhibits a high power factor and reduced thermal conductivity. As a result, an improved value of 0.46 at room temperature has been observed, demonstrating that these simple, abundant, and non-toxic CuS/CuI composites are attractive candidates for thermoelectrics.

Keywords: thermoelectrics; composites; core-shell; environmentally friendly; high performance thermoelectrics

Introduction

The majority of present thermoelectric devices are primarily based on heavy elements like tellurium, bismuth and lead.[1] These well-known toxic and expensive elements cause major constraints on the widespread implementation of thermoelectrics,[1]and as such, the development of new and abundant thermoelectric materials are essential to replace the expensive and toxic elements.[1-3] Such new materials should also possess improved or at least comparable thermoelectric performance as that of well-known "state-of-the-art" compounds for them to become widely used in device fabrication.[4-7]

The thermoelectric efficiency, also known as the "figure of merit" (zT) of a material depends on the electrical conductivity (σ), the Seebeck coefficient (S), and the thermal conductivity (κ). The thermoelectric figure of merit is defined by[8]

$$zT = \frac{S^2 \sigma T}{\kappa} ,\#(1)$$

The primary challenge in optimizing materials is the fact that all these properties (σ, S, and κ) are strongly interrelated[9] and furthermore have different dependences on the carrier density. For illustration, the electrical conductivity of a material increases with an increase in carrier density, which is beneficial for zT, but simultaneously, the Seebeck coefficient decreases, which is detrimental to zT.[9] In addition, the third parameter κ also tends to increase due to the electrical contribution to the thermal conductivity, which is again detrimental to zT. Therefore, careful tuning of these properties is a key factor to achieve improvements in the performance of any thermoelectric material.

Among various schemes that have been shown to effectively enhance zT,developing a multi-phase composite thermoelectric compound is an emerging improvement strategy.[10, 11] These multiphase composites can break the strongly coupled electronic and thermal parameters, which helps to achieve high thermoelectric performances. In this work, copper sulphide (CuS) particles are encapsulated with copper iodide (CuI) in a facile synthesis methodto produce CuS:CuI composites. The composites show highly conductive CuS particles uniformly dispersed in the matrix of CuI, forming an interesting "core-shell type" structure. Thus, the as-formed composites provide a combination of high electrical conductivity (from CuS) and high Seebeck coefficient (from CuI) and as a result, significant enhancements in the zT, with a maximum value of 0.46 (at 300 K), have been observed for the optimised compositions of the composite material. It is predicted that the observed phenomenon is a typical case of energy filtering mechanism commonly observed in different thermoelectric materials.[12-14]

It is wellknown that only very few materials show practically useful zT values at room temperature, and most of these are expensive, toxic and require energy-intensive manufacturing processes.[15-18] Therefore, the developed low-cost and abundant CuS:CuI composites are potential candidates for low-grade heat recovery.

Experimental Section

Synthesis of starting materials-copper sulphide (CuS) and copper iodide (CuI):

Gram-scale CuS particles were produced from elemental Cu and S powders following a previously reported method.[19] Cu (99.9%, Alfa Aesar) and S (99.5%, Alfa Aesar) powders were directly mixed according to the required composition in hydrazine hydrate/water solvent under continuous magnetic stirring at 80 °C for ~ 4 hr. The resulting dark brown particles were washed, collected and dried in an oven at 50 °C. CuI powder was synthesised using an aqueous route by mixing copper sulphate (AR grade, Alfa Aesar) and potassium iodide (AR grade, Alfa Aesar) solutions at room temperatures.

Synthesis of CuI encapsulated CuS particles:

CuI powder was dissolved in acetonitrile (CH_3CN, Alfa Aesar) by ultrasonication to form a transparent solution. Then the CuI solution was slowly added (~ 1 mL each time) into a pestle mortar containing CuS particles with continuous and gentle grinding. The mixing was carried out at ~ 30 (±2) °C to accelerate solvent evaporation. The stepwise addition of CuI solution was carried out until a desired amount of CuI was added to the mixture and finally, CuI encapsulated CuS composites were collected and dried at 50 °C. A schematic illustration of the synthesis is shown in Figure 1. A series of samples of composition CuS:CuI (wt%) = 1:0, 1:0.5, 1:1, 1:2, 1:3, 1:4, 1:5, and 0:1 were prepared for the thermoelectric study.

Characterisation:

Crystal structures of the composites and starting materials were characterised using a Bruker D8 diffractometer with Cu Kα radiation. SEM (Scanning electron microscope) images were recorded using a Hitachi TM3030 SEM equipped with an Oxford X-map energy dispersive X-ray spectrometer (EDX) system. For thermoelectric measurements, thin pellets of the composite samples were obtained from pressing the powders (pressure ~ 12 ton, pressing time ~ 30 min, pellet diameter 16 mm) at room temperature and were cut into bar shapes. The Seebeck coefficient (S) measurements were obtained with a lab built apparatus. The voltage difference (ΔV) and temperature difference (ΔT) between the hot and the cold sides of the samples were used to estimate S by[20]

$$S = -\left(\frac{\Delta V}{\Delta T}\right), \#(2)$$

The electrical conductivity was measured through a standard four probe method. The thermal conductivities of all the samples were measured by a steady state method in a vacuum (10^{-4} mbar) using a home build system. The measurement procedure was carried out according to the parallel thermal conductance method.[21, 22] In a typical measurement, the thermal conductivity of a sample was obtained by measuring the total thermal conductivity (sample + test setup) and the baseline thermal conductivity of the test setup

(no sample). The difference of which gave the sample's thermal conductivity.[22] All the measurements were repeated in order to confirm the reproducibility of the obtained results.

Computational details

The DFT calculations presented throughout this work were performed using the CRYSTAL17 code.[23, 24] The short-range corrected range-separated hybrid Heyd−Scuseria−Ernzerhof (HSE, ω = 0.2 Bohr^{-1})[25-27] functional was employed to approximate the exchange-correlation functional in association with atom-centred Gaussian-type basis sets: copper was described by (86)-(4111)-(41d)G contractions of primitive functions as used in Doll *et al*,[28] iodide by an effective-core pseudo-potential (EC) taken from Doll *et al*,[29]and sulphur by the (86)-(311)G* all-electron basis of Lichanot*et al.*[30] The *s* and *p* shells of iodide were merged for computational efficiency and an all-electron basis set was tested for iodide when extracting the electrostatic potential (full basis information found in the *Supplementary Information* file). For the evaluation of the Coulomb and exchange integrals, the tolerance factor values of 8, 8, 8, 8, and 16 were used (TOLINTEG). The convergence threshold on the self-consistent-field energy was set to 10^6 Ha for single-point and to 10^7 Ha for geometry relaxations. Long range dispersion corrections were included using the semi-empirical D3 approach of Grimme*et al* with Becke-Johnson damping.[31-33] Band structure calculations were performed on optimized geometries along high-symmetry directions obtained using the SeeK-path interface.[34, 35] The diagonalization of the Hamiltonian matrix was conducted in the reciprocal space using Monkhorst-Pack meshes[36] of 15 × 15 × 15 for bulkCuI and11 × 11 × 11 for bulk CuS. The Fermi surface was smeared using a Fermi function[37] and a temperature of 0.001 Ha.Graphical drawings were created using Ovito.[38]

The surfaceswere modelled as two-dimensional slabs, and no three-dimensional periodicity was imposed, which means that no parameter is needed for the vacuum thickness. To characterise the surface, the surface energy (γ) as a measure of the thermodynamic stability has been calculated through the following expression:

$$\gamma = \frac{E(n) - n \cdot E_{bulk}}{2 \cdot A}, \#(3)$$

where$E(n)$ is the energy of the slab containing n-layers, E_{bulk} the energy of the bulk, and A the area of one side of the slab.

The specific adhesion energy, a measure of the gained energy once the interface boundary between two surfaces (s1 and s2) is formed, is given by:

$$\beta_{s1/s2} = \frac{E_{s1} + E_{s2} - E_{s1/s2}}{A}, \#(4)$$

where$E_{s1}$and $E_{s2}$are total energies of the respective slabs and $E_{s1/s2}$ is the final interface energy.

Thermoelectric properties such as the Seebeck coefficient (S), electrical conductivity (σ), and electron contribution to the thermal conductivity (κ_{el}) were computed using the semi-classical Boltzmann transport equation theory and the frozen band approximation, as implemented by Sansone*et al.* in CYRSTAL.[39] The constant relaxation time approximation for carriers was assumed and fixed at 10fs for all systems and temperatures. A dense mesh of up to 120x120x120 k-points was used in the first Brillouin zone for the calculation of transportcoefficients.

Results and discussion

As illustrated in Figure 1, the synthesis procedure is facile and requires no energy-intensive processes. Various compositions of the CuS:CuI composites were prepared by mixing CuS and CuI in the desired quantities. In the process, CuS particles were encapsulated within CuI, to form core-shell type composites. A schematic structure of the pelletised solid composite is shown in figure. In order to explore the effects of CuI encapsulation of CuS particles on the thermoelectric properties of the CuS:CuI composites, CuS:CuI ratios (wt%) of x = 1:0, 1:0.5, 1:1, 1:2, 1:3, 1:4, 1:5, and 0:1 were selected in the formation of the composites. X-ray diffraction patterns of the composites along with the starting materials, CuS and CuI, are shown in Figure 2. The starting materials confirm the single phase formation, which can be indexed to JCPDS card numbers 06-0464 (hexagonal covellite phase CuS) and 06-0246 (cubic phase CuI), respectively. The diffraction patterns of all the composites show well-defined Bragg peaks corresponding to the crystalline planes for CuI, and the presence of minor peaks corresponding to CuS at 32° and 47° can be observed in the composites of 1:1 and 1:2 compositions. The very small intensity of the CuS peaks in the composites could be due to the formation of thick layersof CuI on CuS particles as well as its highly crystalline nature.

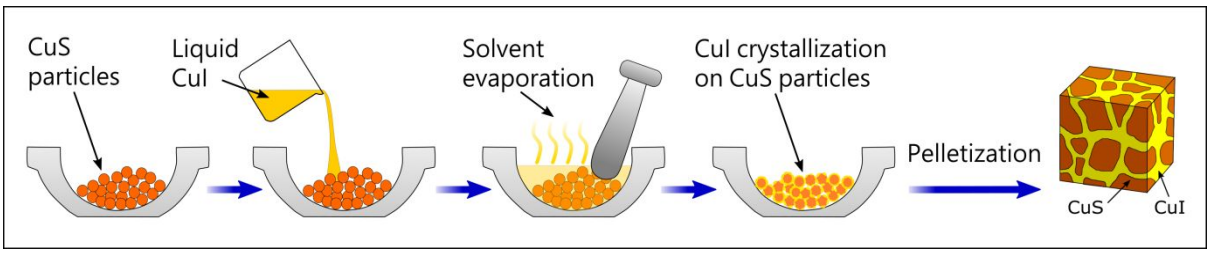

Figure 1.Schematic illustration of the synthesis procedure for CuS:CuI core-shell type composites

When the resulting CuS:CuI composite powders were pressed into solid pellets, the samples show CuI particles distributed in the matrix of CuI as shown by an SEM image (see Figure 3) of a sample with CuS:CuI (wt%)-1:4.The CuI crystallisation on CuS can be confirmed from the well-defined elemental S and I colour distributions in Figure. High resolution images of elemental mapping and the composition are also provided in the Supporting Information (Figure S1).

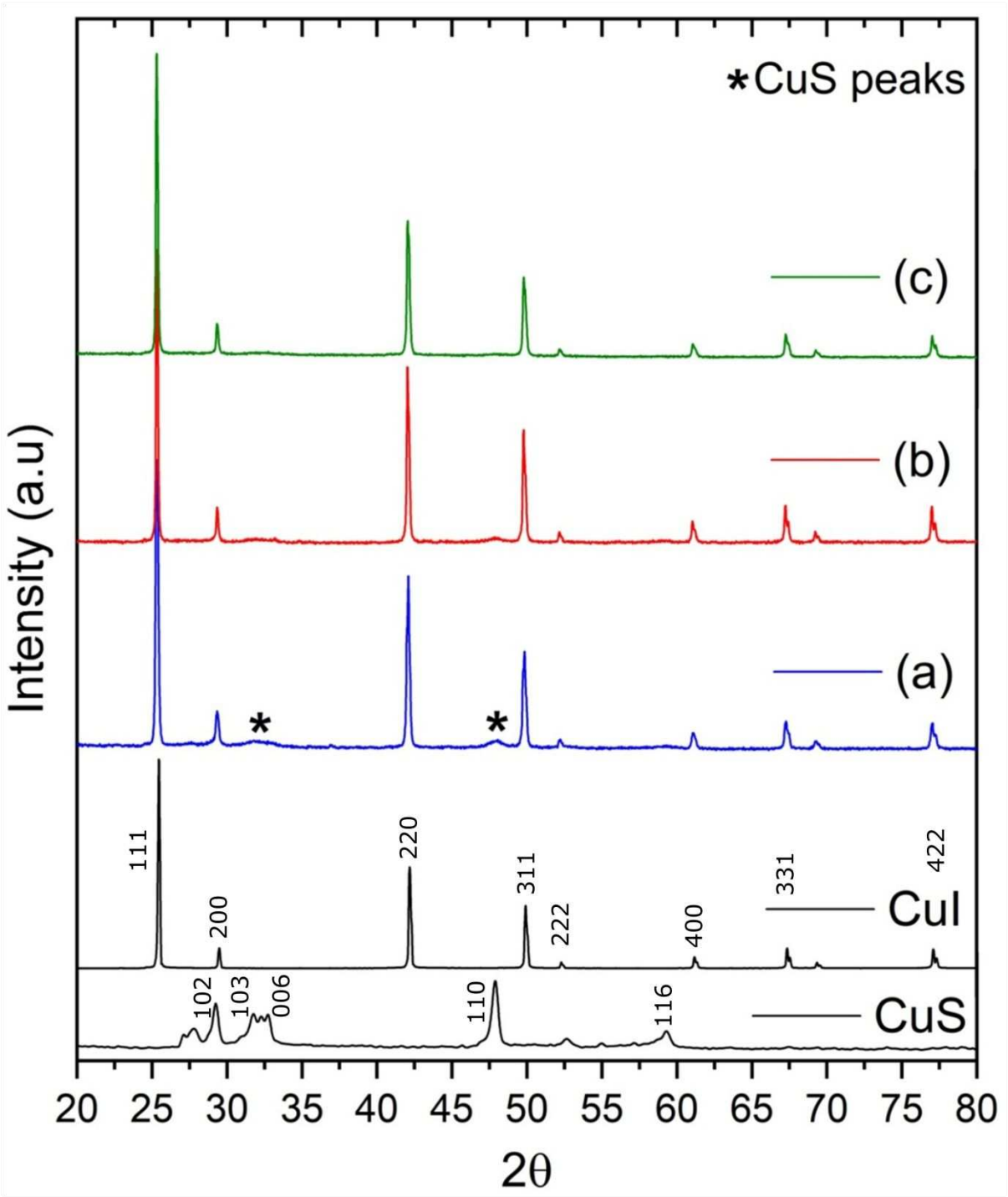

Figure 2.X-ray diffraction patterns of the composites and starting materials, CuS and CuI (patterns a, b, and c correspond to the CuS:CuI composites of composition 1:1, 1:2, and 1:4, respectively).

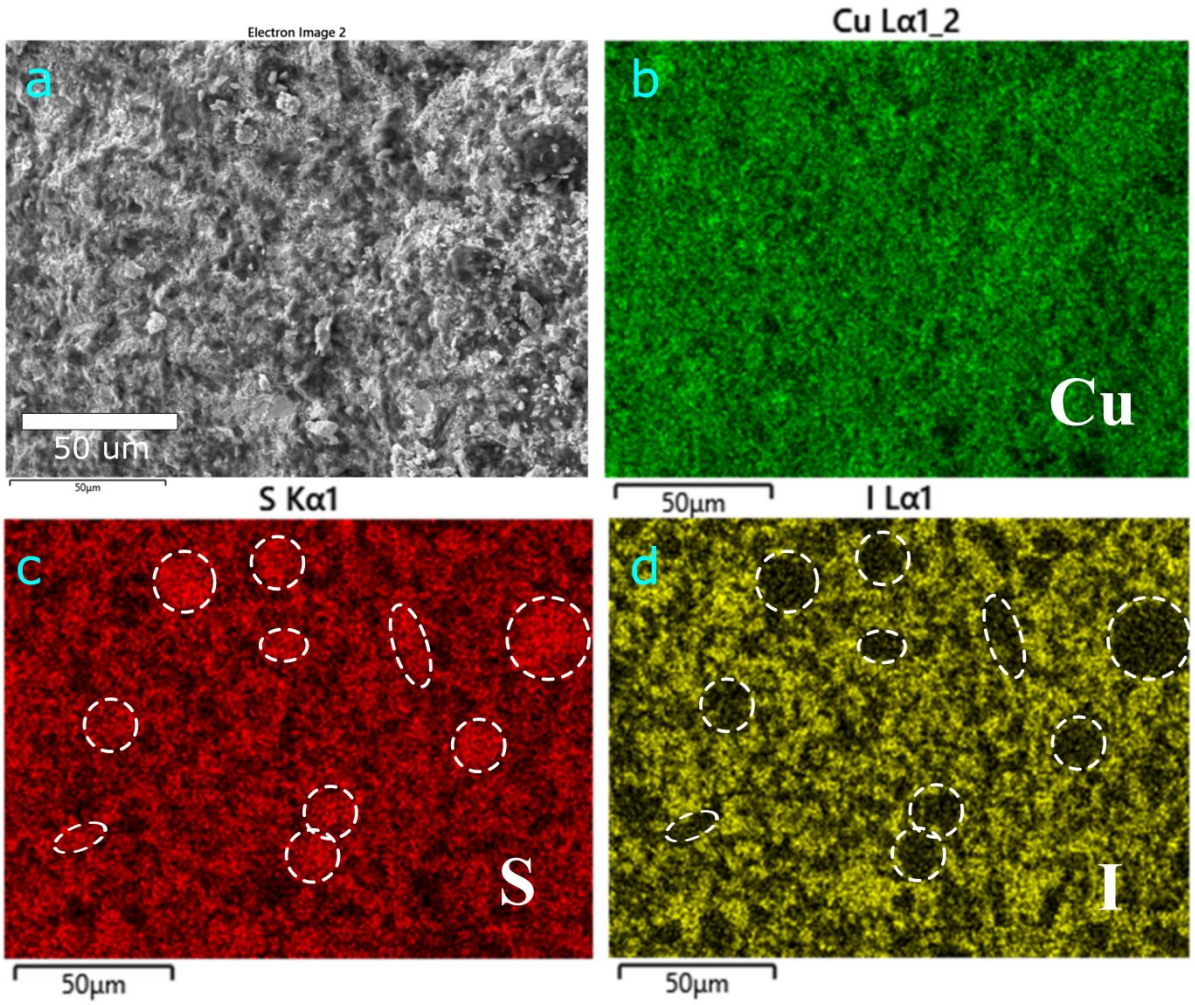

Figure 3.SEM-EDX elemental mapping of a broken solid pellet of CuS:CuI composite sample with CuS:CuI (wt%)-1:4 (b, c, and d are elemental mapping images for Cu, S, and I, respectively). The white dotted regions indicate the presence of larger CuS islands in the sea of CuI.

The choice of the starting compounds CuS and CuI was made owing to their exceptionally different thermoelectric properties. Both CuS and CuIare well-known p-type semiconductors, where CuS exhibits an excellent metallic-like electrical conductivity and CuI achieves a higher Seebeck effect.[40-44] As shown in Figure 4, the difference between the Seebeck coefficient (S) of the starting compounds CuS and CuI was found to be quite large. CuS has a very small S of ~10 μVK^{-1}, whereas CuI exhibits a high S of ~280 μVK^{-1}. With the addition of CuI, initially, to create composites with small quantities ofCuI, no notable changes were observedin the S values. However, after the x=1:2 composition, there was a significant increase in the S, which is mostly dominated by the properties of CuI. In contrast, the electrical conductivity (σ) of CuS decreased with the increase of CuI content. The observed σ of CuS is 1.2 x 10^3 Scm^{-1} but it is only 20.7 Scm^{-1} for CuI. Although the σ of CuS and CuI differ widely, the decrease in σ is slow with the increase of CuI content for the composite compounds, which is a beneficial factor. As a result, the power factor (PF) has

improved in the case of all composites and reached a maximum value of ~1400 μWm^{-1}K^{-2} for the x=1:4 composite.

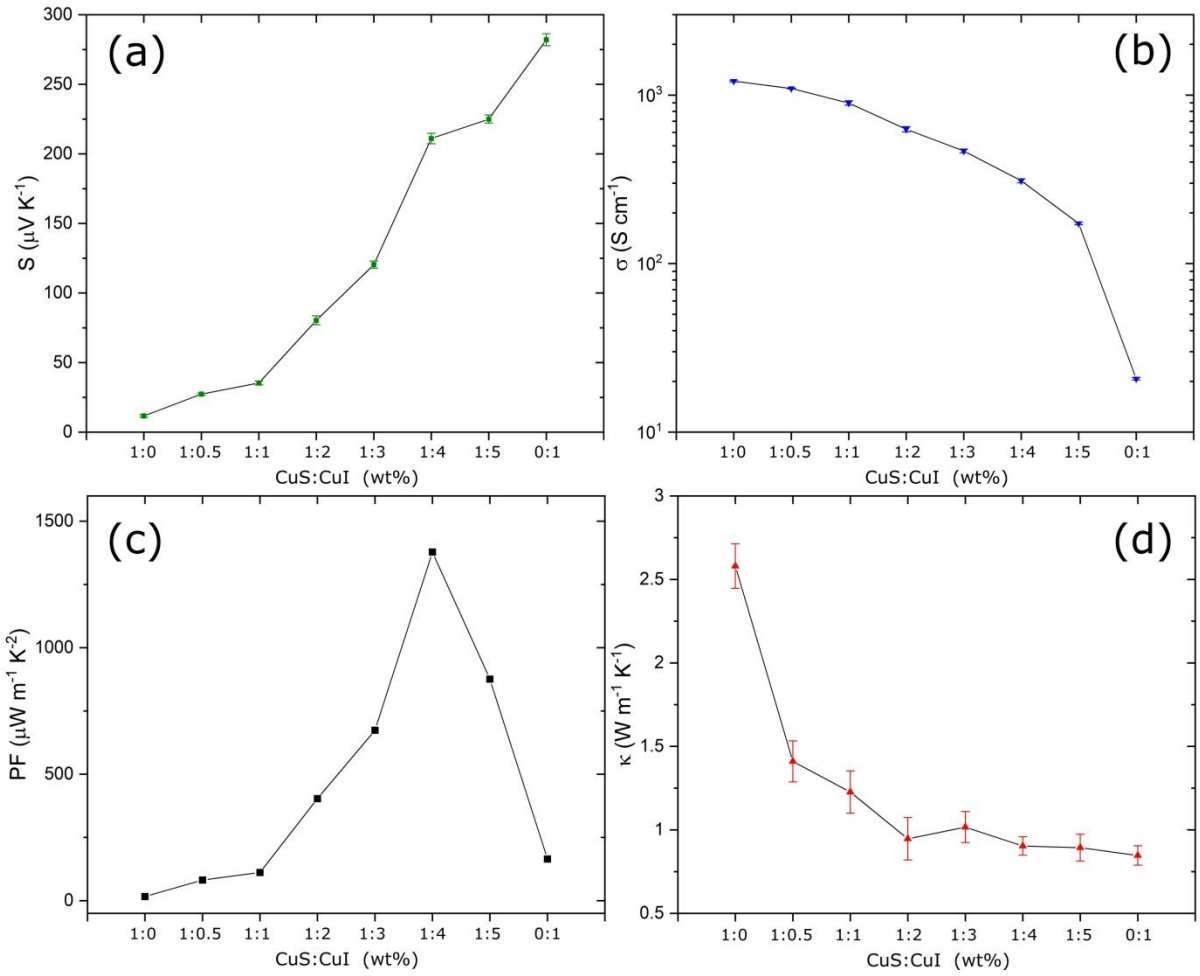

Figure 4.Room temperature Seebeck coefficient (a), electrical conductivity (b), power factor (c), and thermal conductivity (d) of the CuS:CuI composites.

Figure 4d displays the composition dependence of the total thermal conductivity (κ) of the CuS:CuI composites. The κ values of all the composites are lower than that of pristine CuS and similar to CuI. Such reduction in the κ of the composites indicates enhanced phonon scattering at the interfaces of CuS and CuI. Simultaneously, enhanced PF and reduced κ have resulted in a peak zT value of 0.46 at 300 K for x = 1:4 composite (Figure 5). Thus, our presentedresults revealthe enhanced potential of CuS:CuI composite materials for room temperature thermoelectric applications when compared to the individual starting compounds.

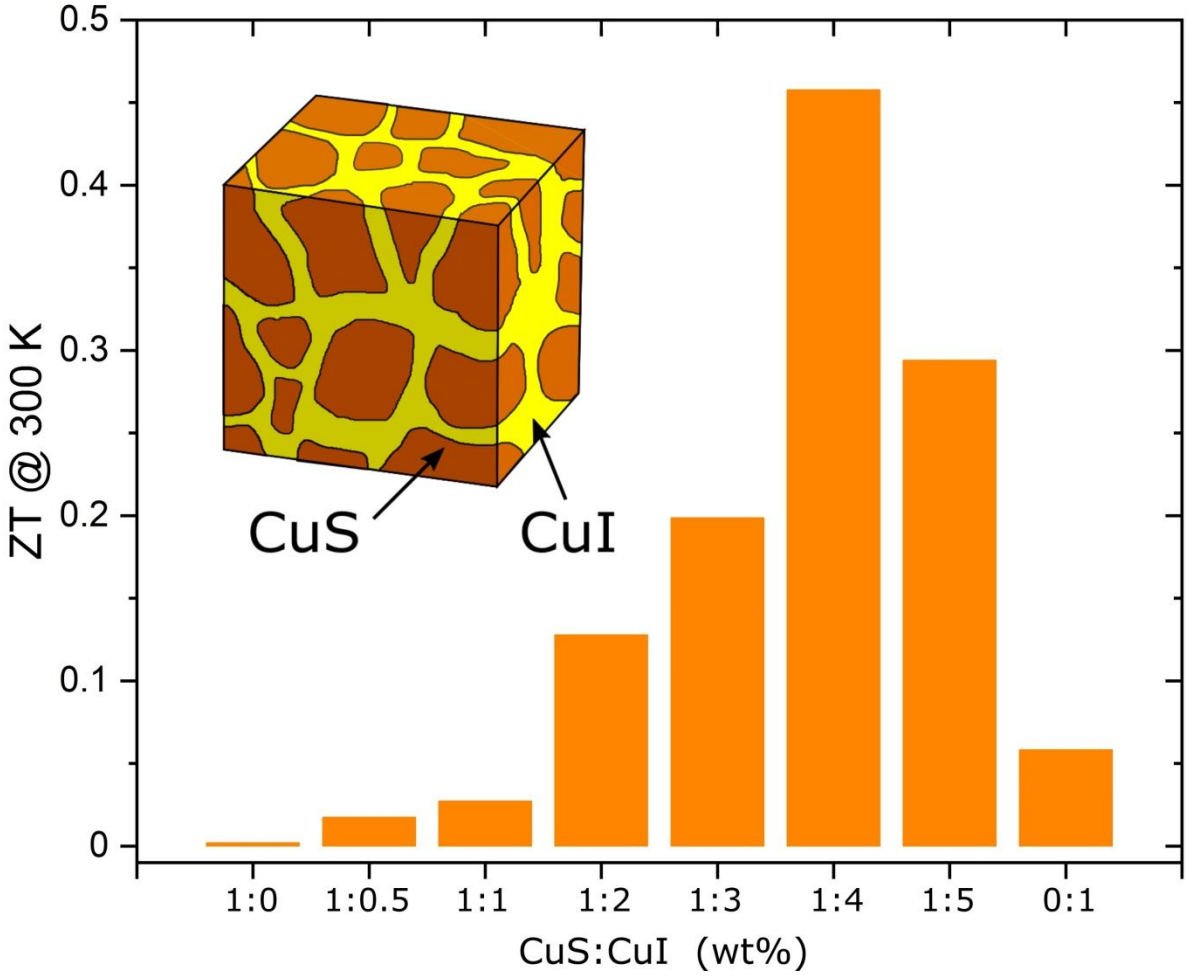

Figure 5.Room temperature zT values of CuS:CuI composites (Inset shows the schematic structure of the composites).

<u>*Calculated bulk crystal structures and electronic properties*</u>

CuS, or covellite, adopts a hexagonal crystal structure (space group 194, P63/*mmc*) with twelve atoms in the unit cell, two of which inequivalent sites for both Cu and S, and a unit cell length of a = b = 3.796 Å and c = 16.36 Å.[45] CuI crystallizes in a cubic (zinc blende) structure (space group 216, F-43m) with eight atoms in the unit cell and one inan equivalent position for each Cu and I. The lattice parameters are measured around 6.1 Å.[46]The calculated structural parameters reproduce the experimental geometry very well, with the lattice parameters reading a = b = 3.807 Å, c = 16.249 Å for CuS and a = 6.037 Å for CuI, obtained using the hybrid HSE functional.

The electronic band structures of CuS and CuI are shown in Figure 6. CuS is correctly described as a conductor, with copper *d*states and sulphur sp^3 states dominating around the Fermi level. In contrast, CuI is an insulator, with a direct band gap found at the Γ-point in reciprocal space, whose Kohn-Sham value equals 3.18 eV, agreeing well with the experimentally measured separation of 3.1 eV.[47] The top of the valence band (VB) is

dominated by admixedcopper *d*and iodide sp^3states, while the bottom of the conduction band is mostly formed by empty copper *sp*-orbitals.

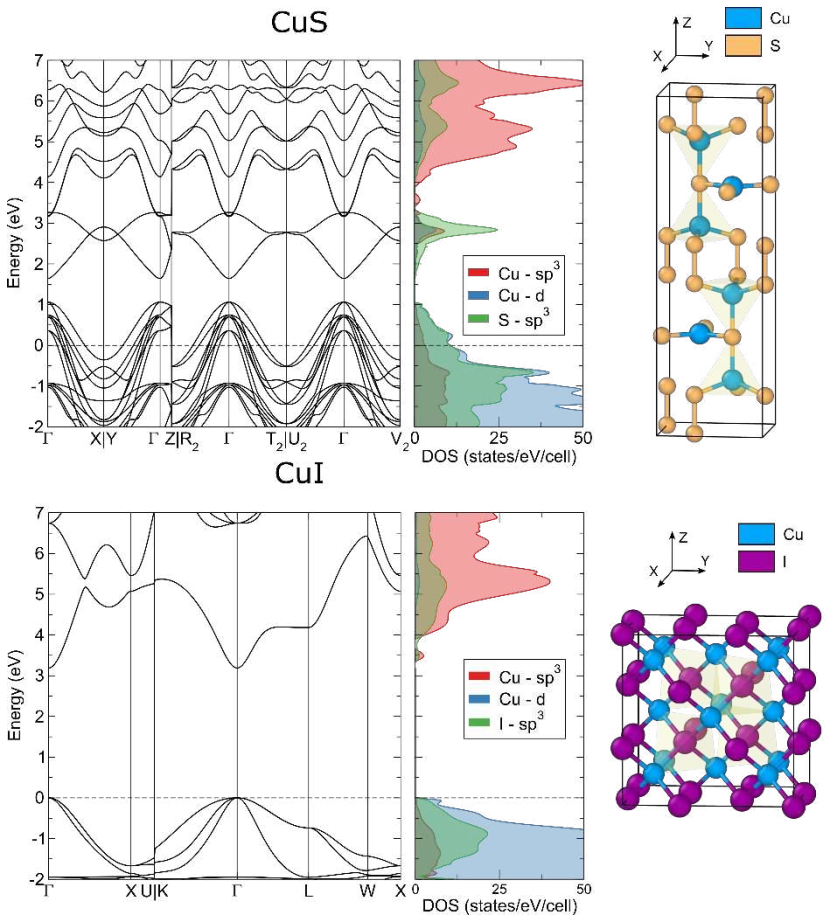

Figure 6. Calculated electronic band structure and orbital-projected densities of states for copper iodide and copper sulphide, together with the corresponding crystallographic unit cells. Results obtained using a hybrid HSE functional.

Calculated bulk thermoelectric properties

The simulated transport properties of bulk CuS and CuI are shown in Figure 7 (individual transport coefficients are plotted in Figure S2). The calculated electronic conductivity and Seebeck coefficient are36.8×10^3 Scm^{-1} and7.47 μVK^{-1} for CuS (values reported along the x-direction for a *p*-type concentration of $1 \times 10^{21} cm^{-3}$at 300 K), and 3.3 Scm^{-1} and 595.5 μVK^{-1} for CuI (values reported for a *p*-type concentration of $1 \times 10^{18} cm^{-3}$ at 300 K), respectively. In CuS, the x- and y-directions are isotropic, while values in the z-direction differ by up to an order of magnitude, e.g., 5.5×10^3 Scm^{-1} for the electrical conductivity (*p*-type concentration of $1 \times 10^{21} cm^{-3}$ at 300 K).

The calculated values are in good agreement with the measurements, reproducing both the order of magnitude as well as the trend between the two compounds, further validating the accuracy of our DFT model. The simulated electronic part of the thermal conductivity of 26.8 CuS reads 26.8 $Wm^{-1}K^{-1}$ in the x- and y-directions and 4.1 $Wm^{-1}K^{-1}$ in the z direction, whereas

it is 0.04 $Wm^{-1}K^{-1}$ for CuI. When compared to experiments (taking an average over the three directions of CuS as 19.2 $Wm^{-1}K^{-1}$), the calculations overestimate the thermal conductivity, which is not necessarily a surprise sincethe model does not include the phonon contributions to the thermal conductivity and phonon scattering processes. However, the relation between CuS and CuI is captured correctly, where CuS demonstrates a much higher thermal conductivity than CuI. What the simulations do reveal is that there is a strong directional dependence in CuS, where values across the xy-crystallographic plane are one order of magnitude higher than those in the z-direction. This potentially serves as further insight when optimizing the thermal conductivity of CuS particles and tuning their properties.

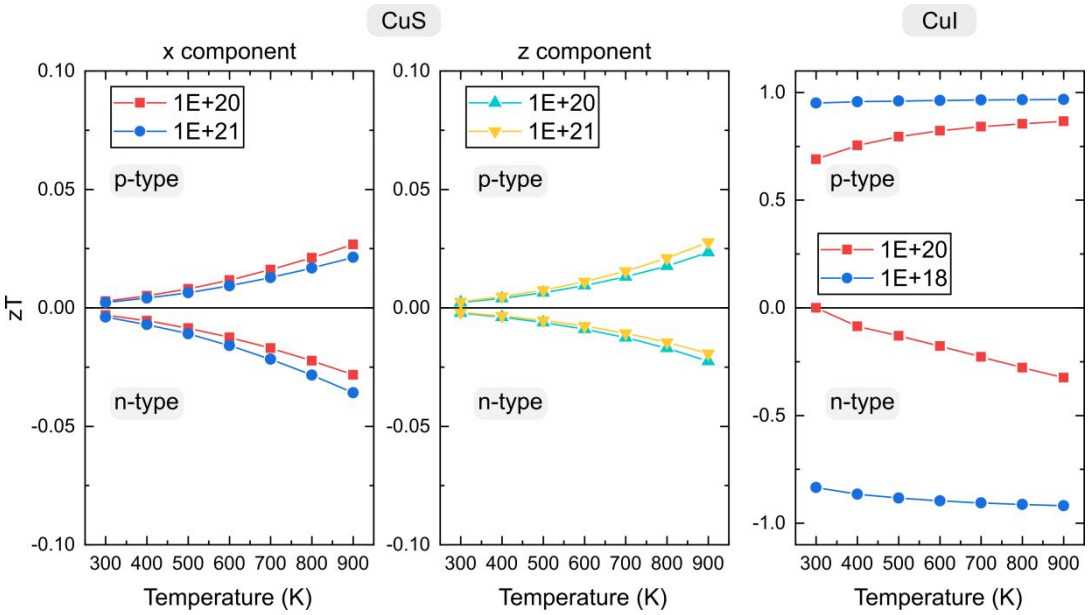

Figure 7. Temperature dependence of the calculated figure of merit for bulk CuS and CuI for both p and n type doping, at the HSE level, obtained from computedSeebeck coefficient (S), electrical conductivity (σ), and electronic contribution to the thermal conductivity (κ_{el}). The ionic contribution to the thermal conductivity has not been taken into account.

With the calculated values discussed above, the dimensionless figure of merit can be estimated. For CuS, a very low zT of 3×10^{-3} at 300 K is obtained, matching well the measured values. No directional dependence of zT is noted for CuS, as the computed variations are too small to make a significant difference in the thermoelectric properties along a preferred crystallographic direction.The zT of CuI is computed at 0.95 at 300 K and a carrier concentration of $1 \times 10^{18} cm^{-3}$, which is much higher than the experimental value of approximately 0.05. The origin of this large discrepancy stems from the underestimated computed thermal conductivity (which neglects phononic contributions). However, if in the calculation of the figure of merit for CuI we replace the computed thermal conductivity by the experimental value (containing all possible contributions, not only the electronic one) of approximately 0.6 $Wm^{-1}K^{-1}$, the zT value is reduced to 0.06 (p-type concentration of $1 \times 10^{18} cm^{-3}$at 300 K), matching the measured figure of merit extremely well. This indicates a

non-negligible lattice contribution to the thermal conductivity of CuI and the strong influence on the final output transport properties. At the same time this confirms that our DFT simulations are able to capture the correct electronic contributions (electrical conductivity, Seebeck coefficient, and thermal conductivity) to the overall transport coefficients of CuI and CuS.

Modelling the interfaces between CuI and CuS

For the subsequent generation and study of the interfaces, we focused on stoichiometric (if available, symmetric) and non-polar surfaces of both copper sulphide and copper iodide. All seven low Miller index cleaved surfaces of CuSare non-polar, so-called type I and II according to the Tasker classification.[48] The CuS (001) and (110) surfaces were selected for further analysis, as they have been reported to be thermodynamically the most stable ones (by DFT)[49] and identified as the dominant planes in the measured XRD spectrum. For CuI, cleaving the relaxed bulk geometry results in only one non-polar surface, the (110) planes, while the (001) and (111) surfaces exhibit a non-vanishing dipole moment across the slab. (For easier distinction between CuS and CuI, we use the (220) surface of CuI in the remaining work, which is equivalent in structure to the (110) due to the isotropy of the system). Such dipolar surfaces undergo significant atomic and structural reorganizations to cancel the intrinsic dipole moment, which are currently outsidethe scope of this study. Surface properties obtained from relaxed slab geometries are reported in Table 1.

Table 1. Calculated properties of chosen CuS and CuI surfaces: surface termination, relaxed surface energy, final slab thickness, electronic band gap. Reported values obtained using the HSE functional. AE – all-electron basis set, EC – effective-core potential. Reported work function, ionization potential, and electron affinity are obtainedusinga bulk-based definition.

Surface label	Termination	Surface energy (J/m^2)	Band gap (eV)	Work function Or IP/EA (eV)
CuS(110)	Cu-S	0.409	Conductive	-5.74
CuS(001)-t1	S	1.054	Conductive	-6.75
CuS(001)-t3	Cu-S	0.413	Conductive	-6.11
CuI(220)	Cu-I	0.182 (AE iodide)	2.63	-5.77/-2.44
		-0.002 (EC iodide)	2.45	N/A

The computed surface energies are in line with earlier theoretical values, e.g. 0.1 Jm^{-2} for the (110) surface of CuI,[50] and 0.4 Jm^{-2} and 0.3 Jm^{-2} for the (001) and (110) surfaces of CuS, respectively (values depending on the functional). For all surface terminations chosen, the structural and electronic properties are converged reasonably wellwith models of more than 1nm thick. However, the calculated band gap of the CuI(220) surface is found to be around

0.5 eV lower than the respective bulk value, originating from surface states presentmainly on the under-coordinated Cu atoms.

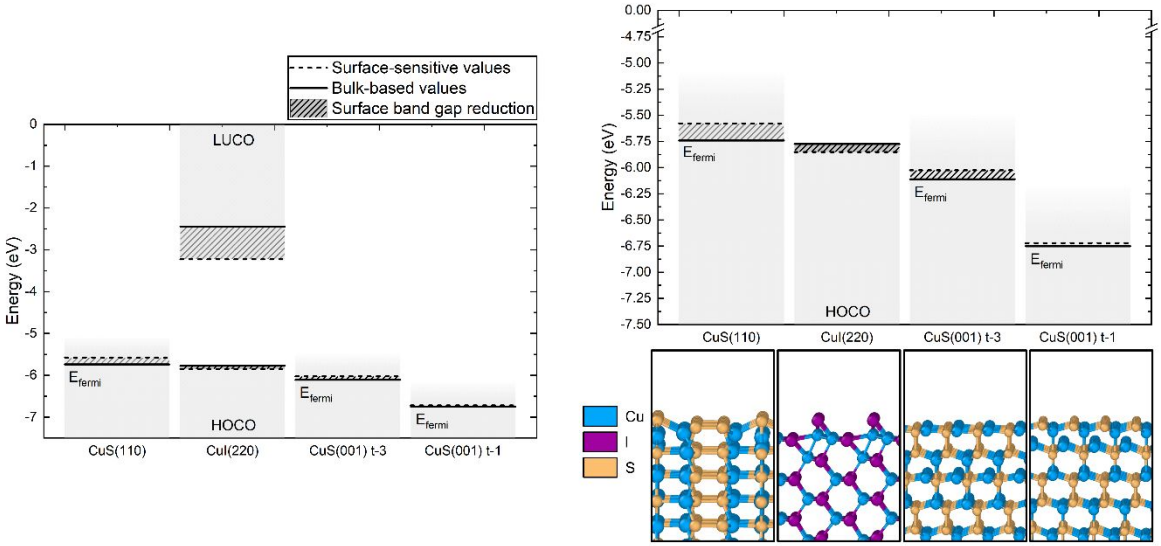

Figure 8. Band alignment based on individual compounds between copper sulphide and copper iodide together with the respective relaxed surface geometries. Values reported for two utilized definitions of the ionization potential and electron affinity, once taken from the respective bulk and once surface values. Values calculated using the HSE functional.HOCO/LUCO denote to the highest occupied/lowest unoccupied crystalline orbital.

The calculated ionization potential (IP, -5.77 eV) of CuI is found to be in good agreement with available experimental IP values of -5.26 eV and -5.05 eV for solution-processed and evaporated CuI samples.[51] The electron affinity (EA) of CuI is computed at -2.44 eV, with no experimental values to compares with, to the best of our knowledge.The work function of CuS is found to be in the range from -5.74 eV to -6.75 eV, in line with earlier works.[52]

From the computed position of the band edges of the chosen individual surfaces, a band alignment scheme can be estimated, as shown in Figure 8. Since we are describing an interface between a metallic and a semi-conducting material, instead of speaking of VB/CB offsets, by definition we are dealing with Schottky barriers. The barrier height is an intrinsic property of the interface and is given by the difference between theFermi level of the metallic contact compound and the semiconductor VB maximum (for the p-type barrier, ϕ_p) or CB minimum (for the n-type, ϕ_n).[53] Based on the analysis undertaken on separate surfaces (and aligned to bulk reference values), the ϕ_p value for an interface between the CuI(220) and CuS(110) surfaces is 0.03 eV, while for a junction between the CuI(220) and CuI(001) surfaces it equals-0.33 eV, indicating that the CuS Fermi level would be located below the VB maximum of CuI. For comparison, the Schottky barriers werealso computed from the ionization potential/electron affinity and work function in the surface-sensitive definition, which is taken as the difference between the vacuum level and highest occupied levels in the slab model.[54] This is done to probe the eventual influence of the surface states on the alignment and future interface creation. The surface-sensitive ϕ_p is found to show the same trend as the bulk-based barriers, with valuesof0.27 eV and 0.17 for the CuI(220)-CuS(110) and CuI(220)-CuS(001) alignments, respectively.

From the alignment of the independent compounds, it is clear that a definite conclusion for the junction type and Schottky barrier height (SBH) between CuI and CuS cannot be reached. Therefore, to gain further information about the interface structure and how it affects the band alignment, explicit interfaces have been simulated. Two heterostructures have been created: one matching the CuI(220) and CuS(110) surfacesand one matching the CuI(220) and CuS(001)-t3 surfaces (labelled as CuI(220)/CuS(110) and CuI(220)/CuS(001), respectively).In both cases, we treat CuI as the epitaxially strained film whose lattice parameters accommodate themselves to those of the CuS substrate. The atomically relaxed structures of the two heterojunction interfaces are shown in Figure 9 and Figure 10.

The calculated adhesion energy, by definition the energy required to separate the two slabs forming the interface tocreate two free surfaces, is$\beta_{CuI(220)/CuS(110)}$ = 0.76 Jm^{-2} and $\beta_{CuI(220)/CuS(001)}$ = 0.79 Jm^{-2}.These energies are very close in magnitude, indicating the stability of both interfaces and, moreover, their likely formation and presence in the experimentally measured samples. The minimal energetic difference most likely arises from the differing binding features at the two interfaces, as well as strain present in the lattice mismatch.

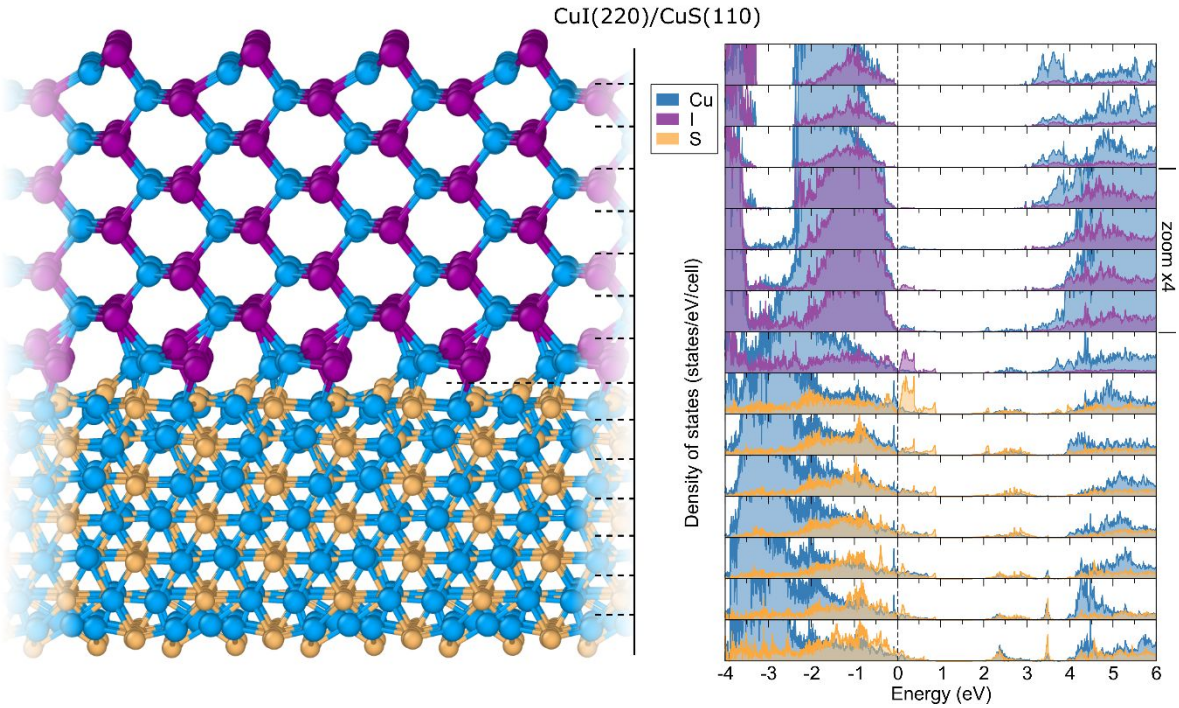

Figure 9. Relaxed atomic structure of the interface formed between the CuI(220) slab acting as a film and the CuS(110) slab acting as the substrate (left) together with the species-resolved layer-projected electronic densities of states (LPDOS, right). Dashed lines in the relaxed structure indicate the layers separation chosen for the LPDOS projections. Zero on the energy axis of LPDOSrefers to the Fermi level of the interface. Values calculated using the HSE functional.

The computed electronic layer-projected densities of states reveal distinct features between the two simulated interfaces. In the bulk region, far enough from the interface as well as bounding surfaces, the electronic structure of pristine CuI (band gap of more than 3 eV) and

CuS (metallic character throughout the slab)is recovered. However, in the interface region, a finite density of states is found in the valence band of the first few layers around the interface of the CuI(220)/CuS(110) heterostructure, in the range of energies which otherwise span the gap of forbidden states (Figure 9). These states are found to propagate 2-3 atomic layers into the structure of CuI and then they decay rapidly onwards. The density of these states is high enough to pin the Fermi level in the vicinity of the VB maximum of the semi-conducting CuI. This can arise from two potentially relevant mechanisms: the pinning of the Fermi level to so-called metal-induced gap states (MIGS) or the pinning of the Fermi level to interface states (Bardeen limit[55]). Interface states are usually characterized by strong localization in the vicinity of the interface, connected to a rapid decay on both sides of the interface. However, this is not the case at the CuI(220)/CuS(110) contact as the states are found present mainly on the CuI side and are broadened out to a maximal width of 1 eV, strongly resembling the shape of the electronic DOS from the CuS side.

One additional option for the origin of the interface states could be the CuI(220) surface states found responsible for the CuI band gap reduction of around 0.5-0.7 eV. However, this was found to originate from predominantly empty Cu surface states positioned around the CB minimum and hence can be ruled out as being present at the discussed interface or responsible for the Fermi level alignment. Taking all of the above into account, it is concluded that Fermi level pinning is present at the CuI(220)/CuS(110) formed heterostructure as a result of newly formed MIGS in the contact region.

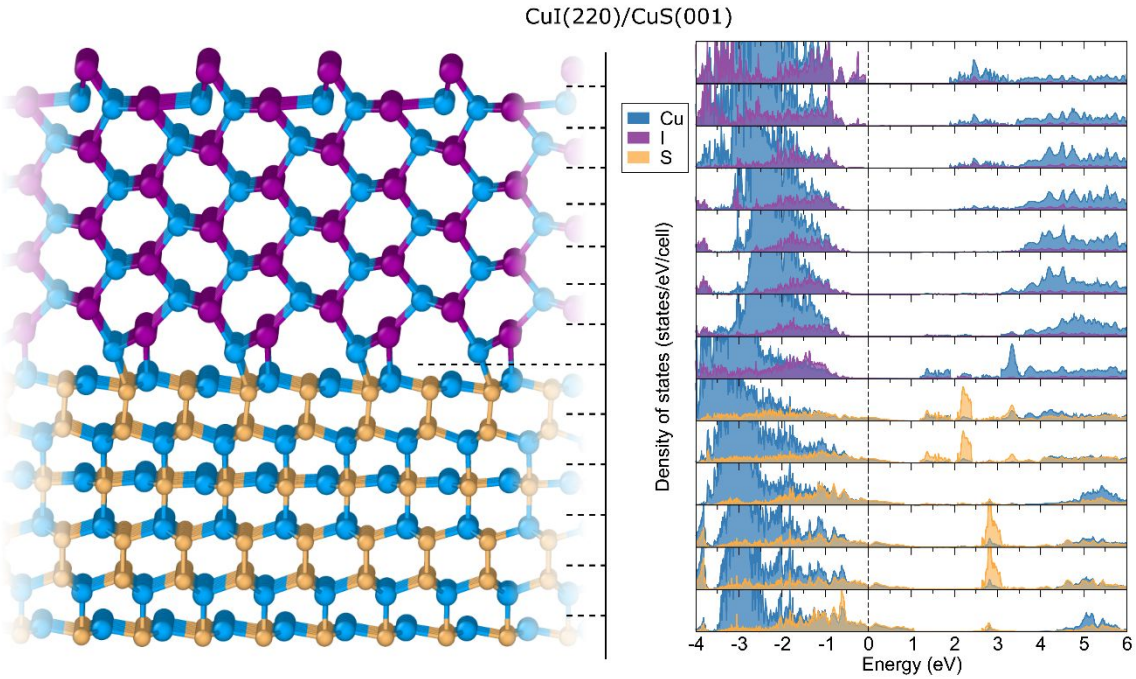

Figure 10. Relaxed atomic structure of the interface formed between the CuI(220) slab acting as a film and the CuS(001) slab acting as the substrate (left) together with the species-resolved layer-projected electronic densities of states (right). Dashed lines in the relaxed structure indicate the layers separation chosen for the LPDOS projections. Zero on the energy axis of LPDOS refers to the Fermi level of the interface. Values calculated using the HSE functional.

In contrast, the CuI(220)/CuS(001) heterostructure does not undergo any protrusion of metallic states into the semi-conducting side, yielding a Schottky barrier with a height of approximately ϕ_p = 0.4 eV between the CuS Fermi level and the VB maximum of the semi-conducting CuI. Moreover, empty states are found on the CuI side of the heterojunction penetrating a maximum of 2-3 layers into the CuI structure. These are mostly confined to Cu states, indicating the presence of newly formed holes when the interface is formed. As a result, the band gap of CuI is reduced to 1.6 eV in the vicinity of the junction, and a Schottky barrier of ϕ_n = 1.2 eV is found between the CuS Fermi level and CuI CB minimum. Further empty states are found on the CuI(220) surface side exposed to vacuum, but these are not of interest for this discussion. Furthermore, the conduction band edge is found to be flat across the semiconductor side, without significant bending occurring near the interface. The outlined results indicate that the CuI(220)/CuS(001) heterostructure displays rectifying characteristics and potential applicability as a diode.

The behaviour of the CuI/CuS interactions is further illustrated by evaluating the charge density difference ($\Delta\rho$), defined as $\Delta\rho = \rho_{s1/s2} - (\rho_{s1} + \rho_{s2})$ and shown in Figure S3, which is useful to estimate the extent and sign of interface dipoles.[56-58] Upon formation, charge redistribution occurs at the interface between the first few layers, with a charge accumulation at the CuI side for both studied systems. Moreover, states at the Fermi level of the CuI(220)/CuS(110) heterostructure are clearly identified, corroborating the LPDOS results of Fermi pinning outlined earlier. This charge transfer results in the formation of an interface dipole which is found to be stronger for the CuI(220)/CuS(110) interface than the CuI(220)/CuS(001) structure. For both structures, the valence band edges are found flat throughout the CuI slab, while the conduction band edge potential is lowered at the interface, i.e., band bending is present towards the metal.

It is also worth noting that the electronic structure of the explicitly treated interfaces is substantially different than the one that would be predicted in the alignment of independent compounds. For many, mostly semi-conducting materials with a minimal lattice mismatch at the interface, the independent alignment produces satisfactory results. However, this is not the case when aligning copper iodide with copper sulphide due to the intricate bonding features at the interface and formation of new states at the interface, which are responsible for altering the position of the Fermi level. Finally, in both simulated instances, the Fermi level of CuS is found positioned higher than the VB maximum of CuI, which cannot be resolved from the alignment based on individual materials.

Based on the given analysis, certain aspects of the improved thermoelectric composite properties may be elucidated. Upon CuI addition to the CuS matrix, layers of CuI are formed on CuS particles, effectively creating a multitude of interfaces at the nanoscale level. Based on the illustrated heterostructure analysis, the final Schottky barrier height, band bending, possibility of Fermi level pinning, and dipole strength depend on the exact nature of the planes coming into contact at the interfaces. However, the injection of electrons from the metal to the semi-conductor impedes the deterioration of the electrical conductivity from

high CuS to low CuI values. Since the thermal conductivity of any given CuS:CuI composite ratio is reduced almost instantly to CuI values, the overall composite zT value is found to be increased, as it depends linearly on the electrical conductivity. As the content of CuI increases, the positive effect on the electrical conductivity wears off, since the bulk content begins to dominate over the interface region and the semi-conducting properties are restored.

Note on computing interface transport coefficients. At this point we refrain from reporting transport coefficients computed via DFT for the individual slabs of CuI and CuS as well as the aforementioned explicitly considered interfaces, despite the fact that we have obtained them. The reasoning for that is two-fold: i) there is an intrinsic difficulty of defining two dimensional electrical and thermal conductivities in relation to their bulk counterparts (see reference of Wu et al.[59]for a detailed discussion of the problem); and ii)the required accuracy and convergence of sampling the reciprocal space and associated electronic band structure via DFT needs to be scrutinized (on which we are preparing a separate discussion in a follow-up work).

Conclusion

The present work has revealed a very simple synthesis route to unique CuS:CuI composites, which are a new and promising p-type high-performance thermoelectric material. The CuS structures encapsulated by CuI in the composites enable simultaneous higher power factors and lower thermal conductivity at room temperature. Density functional theory simulations corroborate further the band alignment and Schottky barrier formation at the interface between CuI and CuS and the positive effect on the overall electrical conductivity of the heterostructure. Depending on the planes in contact at the interface, Fermi level pinning was identified, as well as electron injection from the metal to the semi-conducting side. This reveals the complex interplay between the CuI layers formed on the CuS matrix, where a multitude of interfaces between various crystallographic planes is created, which are not all beneficial for the final output thermoelectric values. The observed maximum zT value of 0.46 suggests great potential for applications at low temperatures from low-cost and abundant materials.

Acknowledgments

The authors are thankful to the Welsh Government (EU European Regional Development Fund) for funding the Rice (Reducing Industrial Carbon Emission) project (Grant Number: 81435). We would also like to acknowledge the assistance provided by Swansea University College of Engineering AIM Facility, which was funded in part by the EPSRC (EP/M028267/1), the European Regional Development Fund through the Welsh Government (80708) and the Ser Solar project via Welsh Government. A.Ž. and N.H.d.L. acknowledge the NWO ECHO grant (712.018.005) for funding. We thank SURF (www.surf.nl) for the support in using the National Supercomputer Snellius.

Conflict of Interest

The authors declare no conflict of interest.

Data Availability Statement

The data that support the findings of this study are available from the corresponding author upon reasonable request.

Bibliography

1. O. Caballero-Calero, J. R. Ares and M. Martín-González, *Advanced Sustainable Systems*, 2021, **5**, 2100095.
2. A. Vora-ud, K. Chaarmart, W. Kasemsin, S. Boonkirdram and T. Seetawan, *Physica B: Condensed Matter*, 2022, **625**, 413527.
3. F. F. Jaldurgam, Z. Ahmad, F. Touati, A. A. Ashraf, A. Shakoor, J. Bhadra, N. J. Al-Thani and T. Altahtamouni, *Journal of Alloys and Compounds*, 2022, **904**, 164131.
4. E. Isotta, J. Andrade-Arvizu, U. Syafiq, A. Jiménez-Arguijo, A. Navarro-Güell, M. Guc, E. Saucedo and P. Scardi, *Advanced Functional Materials*, 2022, **32**, 2202157.
5. G. Ersu, C. Munuera, F. J. Mompean, D. Vaquero, J. Quereda, J. E. F. S. Rodrigues, J. A. Alonso, E. Flores, J. R. Ares, I. J. Ferrer, A. M. Al-Enizi, A. Nafady, S. Kuriakose, J. O. Island and A. Castellanos-Gomez, *ENERGY & ENVIRONMENTAL MATERIALS*, **n/a**, e12488.
6. T. Cao, X.-L. Shi and Z.-G. Chen, *Progress in Materials Science*, 2023, **131**, 101003.
7. A. Liu, H. Zhu, M. G. Kim, J. Kim and Y. Y. Noh, *Advanced science (Weinheim, Baden-Wurttemberg, Germany)*, 2021, **8**, 2100546.
8. M. S. Dresselhaus, G. Chen, M. Y. Tang, R. G. Yang, H. Lee, D. Z. Wang, Z. F. Ren, J.-P. Fleurial and P. Gogna, *Advanced Materials*, 2007, **19**, 1043-1053.
9. J. L. Blackburn, A. J. Ferguson, C. Cho and J. C. Grunlan, *Advanced Materials*, 2018, **30**, 1704386.
10. R. Fortulan and S. Aminorroaya Yamini, *Materials (Basel, Switzerland)*, 2021, **14**.
11. R. Mulla and C. W. Dunnill, *Materials Advances*, 2022, **3**, 125-141.
12. C. Gayner and Y. Amouyal, *Advanced Functional Materials*, 2020, **30**, 1901789.
13. P. P. Murmu, V. Karthik, Z. Liu, V. Jovic, T. Mori, W. L. Yang, K. E. Smith and J. V. Kennedy, *ACS Applied Energy Materials*, 2020, **3**, 10037-10044.
14. A. Pakdel, Q. Guo, V. Nicolosi and T. Mori, *Journal of Materials Chemistry A*, 2018, **6**, 21341-21349.
15. X. Mo, J. Liao, G. Yuan, S. Zhu, X. Lei, L. Huang, Q. Zhang, C. Wang and Z. Ren, *Journal of Magnesium and Alloys*, 2022, **10**, 1024-1032.
16. J. Jiang, H. Zhu, Y. Niu, Q. Zhu, S. Song, T. Zhou, C. Wang and Z. Ren, *Journal of Materials Chemistry A*, 2020, **8**, 4790-4799.
17. C. Yang, D. Souchay, M. Kneiß, M. Bogner, H. M. Wei, M. Lorenz, O. Oeckler, G. Benstetter, Y. Q. Fu and M. Grundmann, *Nature Communications*, 2017, **8**, 16076.
18. J. Coroa, B. M. Morais Faustino, A. Marques, C. Bianchi, T. Koskinen, T. Juntunen, I. Tittonen and I. Ferreira, *RSC Advances*, 2019, **9**, 35384-35391.
19. R. Mulla, D. R. Jones and C. W. Dunnill, *ACS Sustainable Chemistry & Engineering*, 2020, **8**, 14234-14242.
20. R. Mulla, K. Glover and C. W. Dunnill, *IEEE Transactions on Instrumentation and Measurement*, 2021, **70**, 1-7.
21. B. M. Zawilski, R. T. L. IV and T. M. Tritt, *Review of Scientific Instruments*, 2001, **72**, 1770-1774.
22. D. Ding, F. Sun, F. Xia and Z. Tang, *Nanoscale Advances*, 2020, **2**, 3244-3251.
23. R. Dovesi, A. Erba, R. Orlando, C. M. Zicovich-Wilson, B. Civalleri, L. Maschio, M. Rérat, S. Casassa, J. Baima, S. Salustro and B. Kirtman, *WIREs Computational Molecular Science*, 2018, **8**, e1360.
24. R. Dovesi, F. Pascale, B. Civalleri, K. Doll, N. M. Harrison, I. Bush, P. D'Arco, Y. Noël, M. Rérat, P. Carbonnière, M. Causà, S. Salustro, V. Lacivita, B. Kirtman, A. M. Ferrari, F. S. Gentile, J. Baima, M. Ferrero, R. Demichelis and M. D. L. Pierre, *The Journal of Chemical Physics*, 2020, **152**, 204111.
25. J. Heyd, G. E. Scuseria and M. Ernzerhof, *The Journal of Chemical Physics*, 2003, **118**, 8207-8215.
26. J. Heyd and G. E. Scuseria, *The Journal of Chemical Physics*, 2004, **121**, 1187-1192.

27. J. Heyd, G. E. Scuseria and M. Ernzerhof, *The Journal of Chemical Physics*, 2006, **124**, 219906.
28. K. Doll and N. M. Harrison, *Chemical Physics Letters*, 2000, **317**, 282-289.
29. K. Doll and H. Stoll, *Physical Review B*, 1998, **57**, 4327-4331.
30. A. Lichanot, E. Aprà and R. Dovesi, *physica status solidi (b)*, 1993, **177**, 157-163.
31. S. Grimme, J. Antony, S. Ehrlich and H. Krieg, *The Journal of Chemical Physics*, 2010, **132**, 154104.
32. S. Grimme, S. Ehrlich and L. Goerigk, *Journal of Computational Chemistry*, 2011, **32**, 1456-1465.
33. S. Grimme, A. Hansen, J. G. Brandenburg and C. Bannwarth, *Chemical Reviews*, 2016, **116**, 5105-5154.
34. A. Togo and I. Tanaka, *arXiv: Materials Science*, 2018.
35. Y. Hinuma, G. Pizzi, Y. Kumagai, F. Oba and I. Tanaka, *Computational Materials Science*, 2017, **128**, 140-184.
36. H. J. Monkhorst and J. D. Pack, *Physical Review B*, 1976, **13**, 5188-5192.
37. N. D. Mermin, *Physical Review*, 1965, **137**, A1441-A1443.
38. A. Stukowski, *Modelling and Simulation in Materials Science and Engineering*, 2010, **18**, 015012.
39. G. Sansone, A. Ferretti and L. Maschio, *The Journal of Chemical Physics*, 2017, **147**, 114101.
40. G. Dennler, R. Chmielowski, S. Jacob, F. Capet, P. Roussel, S. Zastrow, K. Nielsch, I. Opahle and G. K. H. Madsen, *Advanced Energy Materials*, 2014, **4**, 1301581.
41. A. Liu, H. Zhu, M.-G. Kim, J. Kim and Y.-Y. Noh, *Advanced Science*, 2021, **8**, 2100546.
42. R. Mulla and M. K. Rabinal, *Energy Technology*, 2018, **6**, 1178-1185.
43. R. Mulla and M. K. Rabinal, *Ultrasonics Sonochemistry*, 2017, **39**, 528-533.
44. R. Mulla, D. R. Jones and C. W. Dunnill, *Materials Today Communications*, 2021, **29**, 102738.
45. L. G. Berry, *American Mineralogist*, 1954, **39**, 504-509.
46. R. W. G. Wyckoff and E. Posnjak, *Journal of the American Chemical Society*, 1922, **44**, 30-36.
47. P. Storm, M. S. Bar, G. Benndorf, S. Selle, C. Yang, H. v. Wenckstern, M. Grundmann and M. Lorenz, *APL Materials*, 2020, **8**, 091115.
48. P. W. Tasker, *Journal of Physics C: Solid State Physics*, 1979, **12**, 4977.
49. Á. Morales-García, J. He, A. L. Soares and H. A. Duarte, *CrystEngComm*, 2017, **19**, 3078-3084.
50. J. Zhu, M. Gu and R. Pandey, *Applied Surface Science*, 2013, **268**, 87-91.
51. Y. Peng, N. Yaacobi-Gross, A. K. Perumal, H. A. Faber, G. Vourlias, P. A. Patsalas, D. D. C. Bradley, Z. He and T. D. Anthopoulos, *Applied Physics Letters*, 2015, **106**, 243302.
52. B.-F. Shan, J. Deng and Z.-Y. Zhao, *physica status solidi (b)*, 2021, **258**, 2100268.
53. M. Peressi, N. Binggeli and A. Baldereschi, *Journal of Physics D: Applied Physics*, 1998, **31**, 1273.
54. Y. Hinuma, F. Oba, Y. Kumagai and I. Tanaka, *Physical Review B*, 2012, **86**, 245433.
55. J. Bardeen, *Physical Review*, 1947, **71**, 717-727.
56. G. Di Liberto, S. Tosoni and G. Pacchioni, *Catalysis Science & Technology*, 2021, **11**, 3589-3598.
57. K. Cheng, N. Han, Y. Su, J. Zhang and J. Zhao, *Scientific Reports*, 2017, **7**, 41771.
58. Y. Jiao, A. Hellman, Y. Fang, S. Gao and M. Käll, *Scientific Reports*, 2015, **5**, 11374.
59. X. Wu, V. Varshney, J. Lee, Y. Pang, A. K. Roy and T. Luo, *Chemical Physics Letters*, 2017, **669**, 233-237.